Hindawi
International Journal of Photoenergy
Volume 2023, Article ID 9633843, 13 pages
https://doi.org/10.1155/2023/9633843

Research Article

A Hybrid Energy Storage System Strategy for Smoothing Photovoltaic Power Fluctuation Based on Improved HHO-VMD

Yu Zhang,[1,2] **Yuhu Wu**,[1] **Lianmin Li**,[1] **and Zhongxiang Liu**[1]

[1]*College of Mechanical and Control Engineering, Guilin University of Technology, Guilin 541004, China*
[2]*Guangxi Key Laboratory of Building New Energy and Energy Saving, Guilin 541004, China*

Correspondence should be addressed to Yu Zhang; 17316606@qq.com

Received 23 November 2022; Revised 16 February 2023; Accepted 8 March 2023; Published 4 April 2023

Academic Editor: Mohammad Alghoul

To solve the problems of large fluctuation of photovoltaic output power affecting the safe operation of the power grid, a hybrid energy storage capacity configuration strategy based on the improved Harris hawks optimization algorithm optimizing variational mode decomposition (IHHO-VMD) is proposed. In this strategy, the improved Harris hawk optimization algorithm is used to adaptively select k and α in VMD parameters and decompose the photovoltaic output power and distinguish between correlated and uncorrelated modes. Similarly, the moving average method (MA) is used to extract the continuous component signal in the uncorrelated mode, and it is reconstructed with the related mode as the grid-connected power that meets the national standard. The hybrid energy storage system (HESS) is used to stabilize the fluctuation component signal. The minimum annual configuration cost of the energy storage system is established as the objective function. The simulation results show that the improved algorithm reduces the cost of the hybrid energy storage system by 6.15% compared with the original algorithm, suppresses the power fluctuation, and improves the economy and stability of the system.

1. Introduction

In order to get rid of excessive dependence on fossil energy and accelerate energy transformation, China has proposed the goal of carbon peak and carbon neutrality. Increasing the proportion of photovoltaic grid-connected power generation in the power grid is an important way to achieve this goal [1]. Due to the randomness, intermittence, and periodicity of photovoltaic power generation, the power of the input grid fluctuates greatly, which challenges the stability of the grid.

The photovoltaic system with an energy storage device can effectively solve the problem of photovoltaic (PV) output power fluctuation and improve the stability of the photovoltaic grid [2]. However, too large capacity configuration will increase the system cost, and too small capacity configuration will lead to frequent switching of charging and discharging states of the system and shorten the service life of the energy storage device [3]. Therefore, many scholars have done a lot of research on suppressing photovoltaic fluctuations and HESS capacity configuration. Reference [4] proposed a VMD-based hierarchical configuration method for HESS power. Because the selection of VMD decomposition parameters k and α has not been studied, it is subjective and empirical. Reference [5] used regenerative boiler and battery as HESS and solved the problem of frequent electrode replacement of regenerative electric boiler in a novel way. However, due to high cost and low efficiency, it will produce economic waste. References [6–8] used adaptive wavelet transform to distribute the output power once and obtained the power and energy storage power which satisfied the grid-connected condition. However, the empirical mode decomposition (EMD) proposed in this paper is prone to modal aliasing and poor decomposition effect and cannot accurately separate signals with similar frequencies. In reference [9], the output power of the photovoltaic power generation system is decomposed by ensemble empirical mode decomposition (EEMD). However, after the decomposition of the EEMD algorithm, the noise component of each mode will be increased, so that the center frequency will be higher, which

will lead to poor decomposition and reduction effect. References [10, 11] observed whether the center frequencies of the VMD modes overlapped and then selected the number of modes based on the advantages. But there are no clear measurement criteria; they are subjective. Reference [12] proposed a grid voltage stability analysis framework considering the uncertainty of photovoltaic power generation and load demand and adopted the Monte Carlo simulation. Reference [13] used the hybrid bat search algorithm and artificial neural network method to optimize the current PI controller parameters of the hybrid energy storage system with the minimum objective function as the fitness function. But the bus voltage fluctuation optimization effect is not ideal. Reference [14] mentioned a parameter adaptive VMD method, using the grasshopper optimization algorithm parameters to optimize, by combining kurtosis and correlation coefficient as the optimization function. Reference [15] introduced a hybrid energy storage system composed of gravitational potential energy storage, a battery (BAT), and a supercapacitor (SC) to improve the economy and flexibility of a renewable energy power system. In [16], a capacity configuration method of HESS considering the time scale of decommissioned batteries was summarized. The results of capacity under different discharge times of hybrid energy storage, different time scales of decommissioned power batteries, and different control strategies were considered. In [17], a power limitation algorithm and a SOC correction strategy are proposed to correct the SOC of HESS. Limiting photovoltaic power when power fluctuations exceed the HESS power capacity can improve the net income of photovoltaic and HESS power stations and smooth the performance of PV output power fluctuations. However, due to the limited power capacity of HESS, there will be a decrease in photovoltaic power output and a decrease in the power generation of power plants.

Due to the deficiencies in the above research, this paper proposes a HESS capacity optimization configuration strategy for IHHO-VMD. Firstly, for the problem that the signal decomposition effect is poor due to the subjectivity of VMD parameter selection, IHHO is used to adaptively select k and α in VMD. Then, the Euclidean distance method [18] is used to distinguish the correlation mode and the noncorrelation mode of the photovoltaic output power, and the MA is used to extract the continuous component signal in the noncorrelation mode, which is reconstructed with the correlation mode as the grid-connected power that meets the national standard, and the fluctuation component signal in the noncorrelation mode is suppressed by HESS. Finally, the minimum annual configuration cost of the energy storage system is established as the objective function, and the IHHO-VMD is used to solve the model to obtain the energy storage capacity configuration that meets the requirements.

The main contributions of this work are as follows:

(1) Compared with the original HHO algorithm, the IHHO algorithm can improve the accuracy and iteration speed of the solution process and reduce the economic cost of HESS. The results show that the power of BAT is reduced by 8.54%, the power of SC is reduced by 2.47%, and the economic cost of HESS is reduced by 6.15%

(2) By comparison, the results of this method show that the phenomenon of light abandonment can be reduced, and it is not much different from the original photovoltaic output, which improves the stability of the grid connection

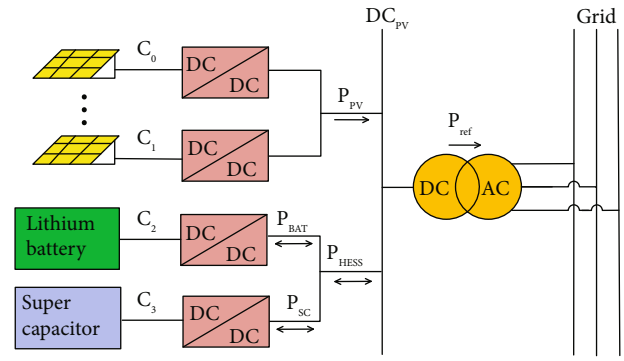

Figure 1: Structure of optical storage system.

2. Photovoltaic Grid-Connected System Model

2.1. Optical Storage System Structure. The optical storage system is composed of PV, HESS, and a power grid, as shown in Figure 1. HESS consists of BAT and SC. P_{PV} is the photovoltaic output power; P_{ref} is the power input to the grid; P_{HESS} is the charging and discharging power of HESS; P_{BAT} is the charge and discharge power of BAT; P_{SC} is the charge and discharge power of SC; C_0, C_1, C_2, and C_3 are DC/DC converters. The photovoltaic array battery and the hybrid energy storage battery are connected to the DC bus through the DC/DC converter. When $P_{HESS} > 0$, HESS is charged; when $P_{HESS} < 0$, HESS discharges.

2.2. Photovoltaic Volatility. The grid-connected power of a photovoltaic power station should meet the fluctuation requirements [19], and the maximum fluctuation limit of active power is shown in Table 1.

In order to quantify the effect of HESS smoothing active power, the PV output power fluctuation index is shown in the following:

$$V_t = \frac{P_{t\ \max} - P_{t\ \min}}{P_{\text{capacity}}} \times 100\%, \tag{1}$$

where V_t represents the photovoltaic power fluctuation rate within the sampling time interval t, $P_{t\ \max}$ represents the maximum output power within the sampling interval t, and $P_{t\ \min}$ represents the minimum output power within the sampling time interval t. P_{capacity} represents the rated installed capacity.

2.3. Power Decomposition Strategy. At present, in most studies on the fluctuation of photovoltaic output power, it is considered that the correlation mode is photovoltaic grid-connected power. The high frequency in the noncorrelation

Table 1: Active power fluctuation requirements of the photovoltaic power station.

Type of power station	1 min maximum fluctuation (kW)	10 min maximum fluctuation (kW)
Small power station	200	Rated installed capacity
Medium-sized power station	Rated installed capacity/5	Rated installed capacity
Large power station	Rated installed capacity/10	Rated installed capacity/3

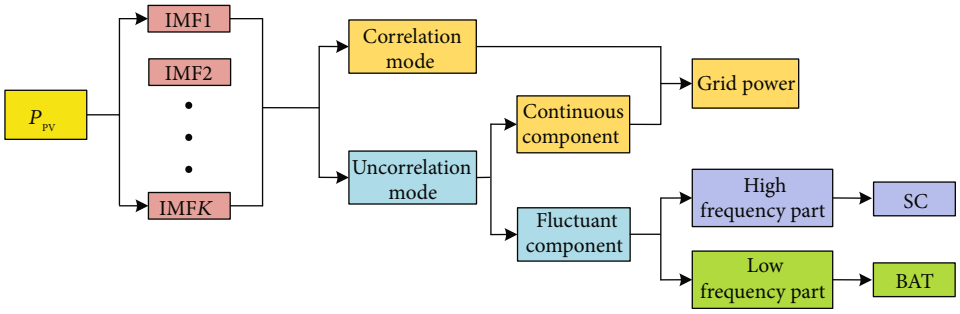

Figure 2: Hybrid energy storage power allocation strategy.

mode is distributed to the power-type energy storage element, and the low frequency is distributed to the energy-type energy storage element. The photovoltaic grid-connected power fluctuation is small, but the grid-connected power is quite different from the original photovoltaic output power, and the phenomenon of light abandonment is more serious. In this paper, P_{PV} has decomposed into IMF1 and IMF2—IMFK intrinsic mode function components by IHHO-VMD; then, the correlated mode and uncorrelated mode are distinguished by Euclidean distance, and MA is used to extract the continuous component signal in the uncorrelated mode for grid connection, and the remaining fluctuations are compensated by SC and BAT; the hybrid energy storage power allocation strategy is shown in (Figure 2).

3. Power Allocation Strategy Based on IHHO-VMD

3.1. Principle of VMD Algorithm. VMD was proposed by Konstantin Dragominetskiy in 2014 [20] to solve the problem that empirical mode decomposition is prone to modal aliasing by iteratively finding the optimal solution of the variational model for complex nonlinear signals. The structure of the variational problem of the VMD algorithm is set as follows. The original signal F can be decomposed into K intrinsic IMF instructions, $u_k(t)$ with central frequency and limited bandwidth, and $u_k(t)$ has a certain sparsity to ensure that the sum of the estimated bandwidths of each $u_k(t)$ is the smallest. The constraint condition is that the sum of F, and all $u_k(t)$ is equal [21]. The variational constraint is established by the following equation:

$$\begin{cases} \left\{ \min_{\{u_k\}\{\omega_k\}} \left\{ \sum_{k=1}^{k} \left\| \partial_t \left[\left(\delta(t) + \frac{j}{\pi t} \right) * u_k(t) \right] e^{-j\omega_k t} \right\|_2^2 \right\} \right. \\ \left. \text{s.t.} \sum_{k=1}^{k} u_k(t) = f(t), \right. \end{cases} \tag{2}$$

where u_k is the decomposed modal component, ω_k is the center frequency of each modal component, $\delta(t)$ is the unit impulse function, k is the number of decomposition modes, $*$ is a convolution symbol, and $f(t)$ is the original signal.

To solve the above constrained variational problem, a quadratic penalty term α and a Lagrangian multiplier λ are used to transform the constrained problem into a nonconstrained solution problem. The augmented Lagrangian multiplier is shown in the following:

$$\begin{aligned} L(\{u_k\}, \{w_k\}, \lambda) = \alpha \sum_k \left\| \partial_i \left[\left(\delta(t) + \frac{j}{\pi t} \right) * u_k(t) \right] e^{-jw_k t} \right\|_2^2 \\ + \left\| f(t) - \sum_k u_k(t) \right\|_2^2 \\ + \left(\lambda(t), f(t) - \sum_k u_k(t) \right). \end{aligned} \tag{3}$$

The alternating multiplier algorithm (3) is used to iteratively update the modal components u_k, the center frequency ω_k, and the Lagrange multiplier λ, and finally, the optimal solution of the augmented Lagrange multiplier is obtained. The update methods of u_k, ω_k, and λ are shown in Equations (4)–(6), respectively,

$$\hat{u}_k^{n+1}(\omega) = \frac{\hat{f}(\omega) - \sum_{i \neq k} \hat{u}_i(\omega) + \left(\hat{\lambda}(\omega)/2 \right)}{1 + 2\alpha(\omega - \omega_k)^2}, \tag{4}$$

$$\omega_k^{n+1} = \frac{\int_0^\infty \omega \left| \hat{u}_k^{n+1}(\omega) \right|^2 d\omega}{\int_0^\infty \left| \hat{u}_k^{n+1}(\omega) \right|^2 d\omega}, \tag{5}$$

$$\hat{\lambda}^{n+1}(\omega) = \hat{\lambda}^n(\omega) + \tau \left(\hat{f}(\omega) - \sum_k \hat{u}_k^{n+1}(\omega) \right), \tag{6}$$

where τ is the noise tolerance of λ. In the case that the decomposed signal does not contain strong noise, generally only the quadratic penalty factor α is used instead of the Lagrange multiplier λ, and τ should be set to 0 to disable λ.

The VMD algorithm will iterate until the convergence error ε satisfies the following equation:

$$\sum_k \frac{\left\|\widehat{u}_k^{n+1} - \widehat{u}_k^n\right\|_2^2}{\left\|\widehat{u}_k^n\right\|_2^2} < \varepsilon. \tag{7}$$

Due to the principle of the VMD algorithm, it is necessary to set parameters artificially when decomposing the signal: the number of modes K and the binomial penalty term α . In the traditional VMD algorithm, the values of K and α are not accurate, which will lead to underdecomposition or overdecomposition of the original signal, resulting in the unreasonable allocation of energy storage power in the system. Therefore, this paper uses intelligent algorithms to solve the parameter combination (k, α) in the VMD algorithm, which can adaptively adjust the VMD parameters according to the change characteristics and complexity of the signal, so as to solve the problem of relying on subjective judgment.

3.2. The Harris Hawk Optimization Algorithm. The HHO algorithm is a naturally inspired algorithm proposed by Heidari et al. [22] in 2019, which is derived from observing the pursuit and escape behavior between the Harris eagle and its prey (rabbit). The algorithm has been widely concerned since it was proposed. Mathematical formulas are used to simulate the strategy of capturing prey under different mechanisms. In HHO, the Harris hawk chooses the solution, and the prey approaches the optimal solution with iteration. The HHO algorithm includes four stages [23].

The Harris hawk is first in a waiting state, carefully checking and monitoring the search space (lb, ub) to find prey and then maintaining an appropriate balance between exploration and exploitation. Finally, according to the detection of the previous stage, the raid is performed to attack the expected prey, while the prey tries to escape from danger. According to the escape and chase, the HHO algorithm proposes four strategies to simulate the attack behavior, referring to the formula in [24].

3.2.1. Soft Siege. Under this search strategy, the prey has enough energy to escape, and the position is updated by the following equation:

$$\begin{cases} X(t+1) = \Delta X(t) - O|JX_{\text{rabbit}}(t) - X(t)|, \\ J = 2(1-r), \\ \Delta X(t) = X_{\text{rabbit}}(t) - X(t), \end{cases} \tag{8}$$

where $X(t+1)$ denotes the position of the Harris hawk at the next moment, $X(t)$ denotes the current position of the eagle, $\Delta X(t)$ represents the difference between the current position of the prey and the eagle, $X_{\text{rabbit}}(t)$ represents the position vector of prey, O is the prey escape energy, J represents the random jump intensity of the prey escape process and r is a random number between 0 and 1.

3.2.2. Hard Enclosure. It indicates that the prey energy is not abundant, and there is no way to jump out of the enclosure, so it is surrounded by hardness. The expression is shown in the following:

$$X(t+1) = X_{\text{rabbit}}(t) - O|\Delta X(t)|. \tag{9}$$

3.2.3. Gradual Rapid Subduction Soft Encirclement. This indicates that the prey is energetic and escapes successfully from the enclosure. At this point, you need to combine Levy flights to update the location of the prey:

$$\begin{cases} Y = X_{\text{rabbit}}(t) - O|\text{JX}_{\text{rabbit}}(t) - X(t)|, \\ Z = Y + S \times \text{Levy}(D), \end{cases} \tag{10}$$

where Levy is the flight expression, D and S are the number and random vector needed to solve Levy flight, Z represents the eagle based on the Levy flight mode, and Y represents the eagle's next action assessment indicator.

$$X(t+1) = \begin{cases} Y, & f(Y) < f(X(t)) \\ Z, & f(Z) < f(X(t)) \end{cases}. \tag{11}$$

3.2.4. Gradual Fast Subduction Hard Encirclement. Prey energy is not abundant, and there is no way to jump out of the enclosure. Therefore, a progressive, fast dive hard encirclement is required, and the position is updated as follows:

$$\begin{cases} Y = X_{\text{rabbit}}(t) - O|\text{JX}_{\text{rabbit}}(t) - X_m(t)|, \\ Z = Y + S \times \text{Levy}(D), \end{cases} \tag{12}$$

where $X_{\text{m}}(t)$ denotes the value corresponding to each dimension of all individuals.

3.3. Multistrategy Improved the Harris Hawk Optimization Algorithm (IHHO). Although the existing HHO improvement strategy improves the exploration and optimization performance of the algorithm to a certain extent, it generally only improves or changes the energy reduction method for a certain update strategy in the HHO algorithm and does not effectively avoid the blindness of global and local optimization. In view of the above problems, reference [25] proposed a multistrategy improved HHO that combines the Cauchy mutation, random shrinkage exponential function, and adaptive weight.

3.3.1. The Cauchy Variation. Aiming at the problem that the HHO optimization algorithm is easy to fall into local optimal value, the global search ability of the HHO algorithm is improved. Combined with the Cauchy operator, the Cauchy distribution function mutation effect is used to optimize

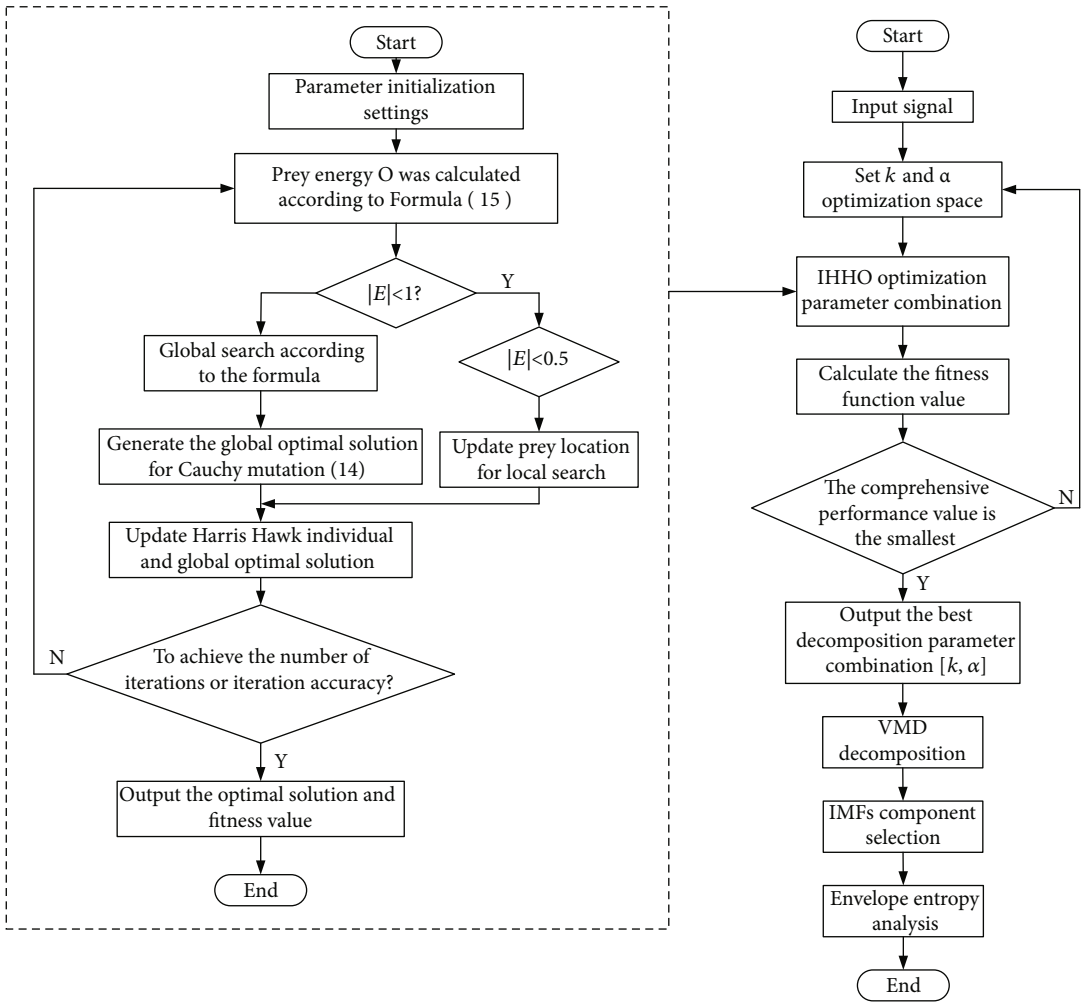

Figure 3: IHHO-VMD flow chart.

the global object. The standard Cauchy distribution function formula is as follows:

$$f(x) = \frac{1}{\pi}\left(\frac{1}{x^2+1}\right). \tag{13}$$

The Cauchy function decreases gently from the peak to both sides. After updating the position by Cauchy mutation, the Harris hawk is constrained by the local extreme point and can jump out of the local extreme. The mathematical model of the Cauchy mutation updates the optimal solution to obtain the current global optimal solution X_{best} by the following formula:

$$X'_{\text{best}} = X_{\text{best}} + X_{\text{best}} \times \text{Cauchy}(0,1). \tag{14}$$

3.3.2. Random Shrinkage Exponential Function. In the HHO algorithm, the size of prey energy O plays the role of adjusting and transiting global search and local exploitation. The linear decrease of O from the maximum to the minimum does not effectively describe the real process of hunting by the Harris eagle groups in nature. Therefore, a modified energy linear decreasing regulation mechanism is proposed to fuse the random shrinkage exponential function with the decreasing process of human prey energy O:

$$O = 2O_0\left(2\,\text{rand} \times \exp\left(-\left(\frac{\pi}{2} \times \frac{t}{T}\right)\right)\right). \tag{15}$$

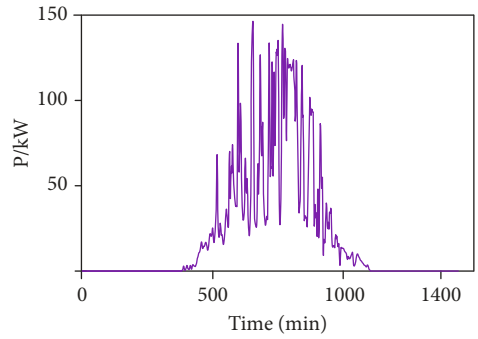

Figure 4: The original photovoltaic output curve of the day.

3.3.3. Adaptive Weight. In order to improve the local mining ability of the algorithm, the neighborhood of the prey location is updated to find a better solution; this paper introduces an adaptive weight method. By fusing adaptive weight factor ω, the algorithm has better local mining ability. The adaptive weight formula and the prey position update are shown in the following formulas:

$$\omega = \sin\left(\frac{\pi \times t}{2T} + \pi\right) + 1, \tag{16}$$

$$X'_{\text{rabbit}} = \omega \times X_{\text{rabbit}}, \tag{17}$$

where T is the maximum number of iterations and t is the current number of iterations.

3.4. Selection of Adaptive Function. The parameters of VMD are self-selective, and the values of noise tolerance τ and convergence error ε have no obvious influence on the reconstruction accuracy of the decomposed signal, which is generally set as the default values $\tau = 0.1$ and $\varepsilon = 10^{-6}$. In order to use IHHO to optimize the VMD critical decomposition parameters, it is necessary to construct a fitness function. The fitness function contains two elements: the number of modes k and the quadratic penalty factor α, which have a significant impact on the VMD decomposition results. The improved Harris eagle optimization algorithm can be used to find the optimal values of parameters k and α.

In this paper, envelope entropy (EE) is used as the IHHO fitness function, and the envelope entropy reflects the sparse characteristics of the signal. Strong coefficient characteristics, small envelope entropy, and the coefficient characteristic are weak, the envelope entropy is big, and envelope information entropy is shown in the following equation:

$$p_{i,j} = \frac{\text{IMF}_{i,j}}{\sum_{j=1}^{N} \text{IMF}_{i,j}}, \tag{18}$$

where $\text{IMF}_{i,j}$ represents the envelope amplitude of the jth sampling point of the ith modal component after VMD decomposition, N is the length of the modal component signal p_{i}, and $_j$ is the normalized modal component envelope:

$$\text{IMF}_{\text{EE}}(i) = -\sum_{j=1}^{N} p_{i,j} \log_2\left(p_{i,j}\right), \tag{19}$$

where $\text{IMF}_{\text{EE}}(i)$ represents the MEE of the ith modal component.

Figure 3 is the IHHO-VMD flow chart using MEE as the fitness function.

4. Verify the Effectiveness of IHHO-VMD

In order to verify the effectiveness of the proposed IHHO-optimized VMD, the original photovoltaic output power is decomposed by IHHO-VMD, VMD, and EMD, respectively. The photovoltaic power plant with installed capacity of 150 kW in Gansu is selected, and the photovoltaic power data on June 28 is taken as the research object. The photovoltaic output curve of this day is shown in Figure 4.

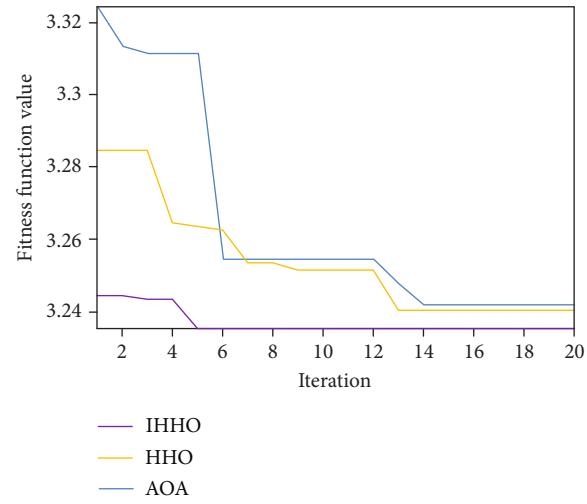

Figure 5: Comparison of fitness function values.

Table 2: The optimum parameters of each algorithm.

Algorithm	k	α
AOA-VMD	6	5755
HHO-VMD	9	5570
IHHO-VMD	10	6440

The analysis of Figure 4 shows that the maximum power of photovoltaic output is 145.3 kW, and the maximum fluctuation rate of photovoltaic within 1 min is 64.8%. According to China's grid-connected photovoltaic power station standard, a 1 min photovoltaic fluctuation rate limit of 20% and a 10 min photovoltaic fluctuation rate of 100% are required to meet the requirements. However, the 1 min PV fluctuation rate is much higher than the upper limit standard of 20%, and the power supply reliability is low, which affects the safe operation of the power grid. It is necessary to stabilize and decompose the P_{PV} to meet the grid-connected requirements.

4.1. Intelligent Algorithm Comparative Analysis Experiment. In order to verify the advantages of the IHHO algorithm, the arithmetic optimization algorithm (AOA), HHO, and IHHO algorithms are used to optimize the VMD parameters. The number of iterations is shown in Figure 5.

The data depicted in Figure 5 reveals that the IHHO algorithm exhibits a minimum fitness function value of 3.236 in the 5th iteration. In contrast, the HHO algorithm demonstrates a minimum fitness function value of 3.240 in the 13th iteration, and the AOA algorithm shows a minimum fitness function value of 3.242 in the 14th iteration. These results indicate that the IHHO algorithm outperforms the other algorithms in both speed and accuracy for solving the problem.

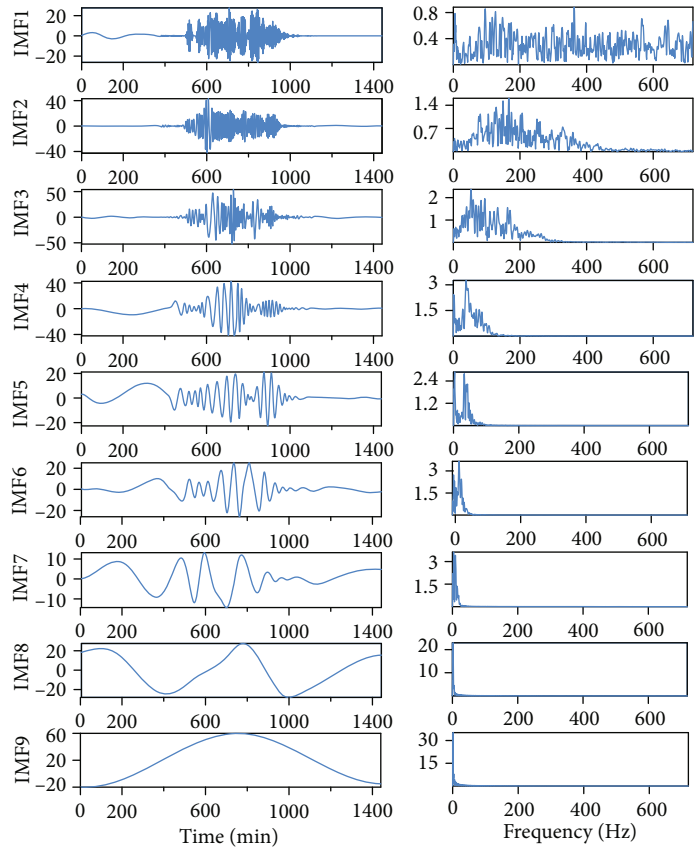

Figure 6: EMD decomposition results.

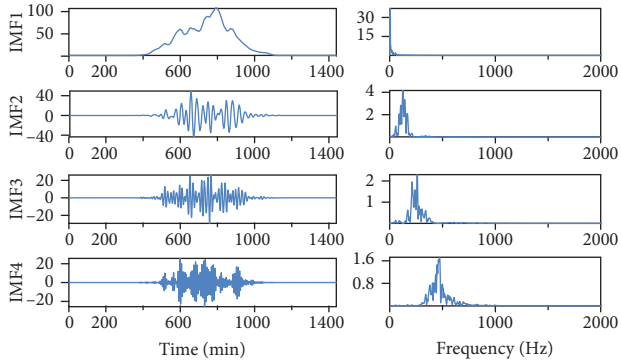

Figure 7: VMD decomposition results.

4.2. Power Decomposition Comparative Analysis Experiment. In order to further verify the superiority of the parameter optimization VMD algorithm proposed in this paper, parameter optimization VMD, VMD, and EMD [26] are used to decompose P_{PV}. The optimal parameter combination $[k, \alpha] = [10, 6440]$ can be obtained by iterative calculation of the IHHO algorithm in Table 2. And the Hilbert transform is performed on the decomposed IMF.

Figure 6 shows the time domain and frequency domain of the modal components obtained by the decomposition of P_{PV} by EMD. Nine modal components are obtained. It can be seen that the different frequency components are mixed seriously, and there are more harmonics. IMF1 and IMF2 almost cover the whole frequency band, and the high- and low-frequency components are not easy to distinguish.

Figure 7 shows the decomposition of P_{PV} using VMD under the default parameters $K = 4$, $\tau = 0.1$, $\varepsilon = 10^{-6}$, $\alpha = 2000$. As shown in the figure, VMD decomposition is better than EMD decomposition, and the modal aliasing phenomenon is not obvious, which is better than being unable to select K and α while modal aliasing still exist. Figure 8 shows that using IHHO to optimize VMD to adaptively search for the best decomposition parameters, the best parameter combination $[k, \alpha] = [10, 6440]$ is obtained, the mode mixing phenomenon is less obvious, and the amplitude is stronger. Therefore, compared with EMD and VMD, the parameter-optimized VMD can better complete the reasonable allocation of HESS power by distinguishing high- and low-frequency components.

4.3. Selection of Correlated and Uncorrelated Modes

4.3.1. Selection Analysis of Related Modes. According to the Euclidean distance theorem in reference [27], the correlated modes and uncorrelated modes are selected. The smaller the d is, the more relevant the submode component is to the original signal. The correlation mode can be determined by evaluating the slope between the Euclidean distance between the two adjacent submodes and the original signal. If the slope between submode j and submode $j + 1$ is the largest,

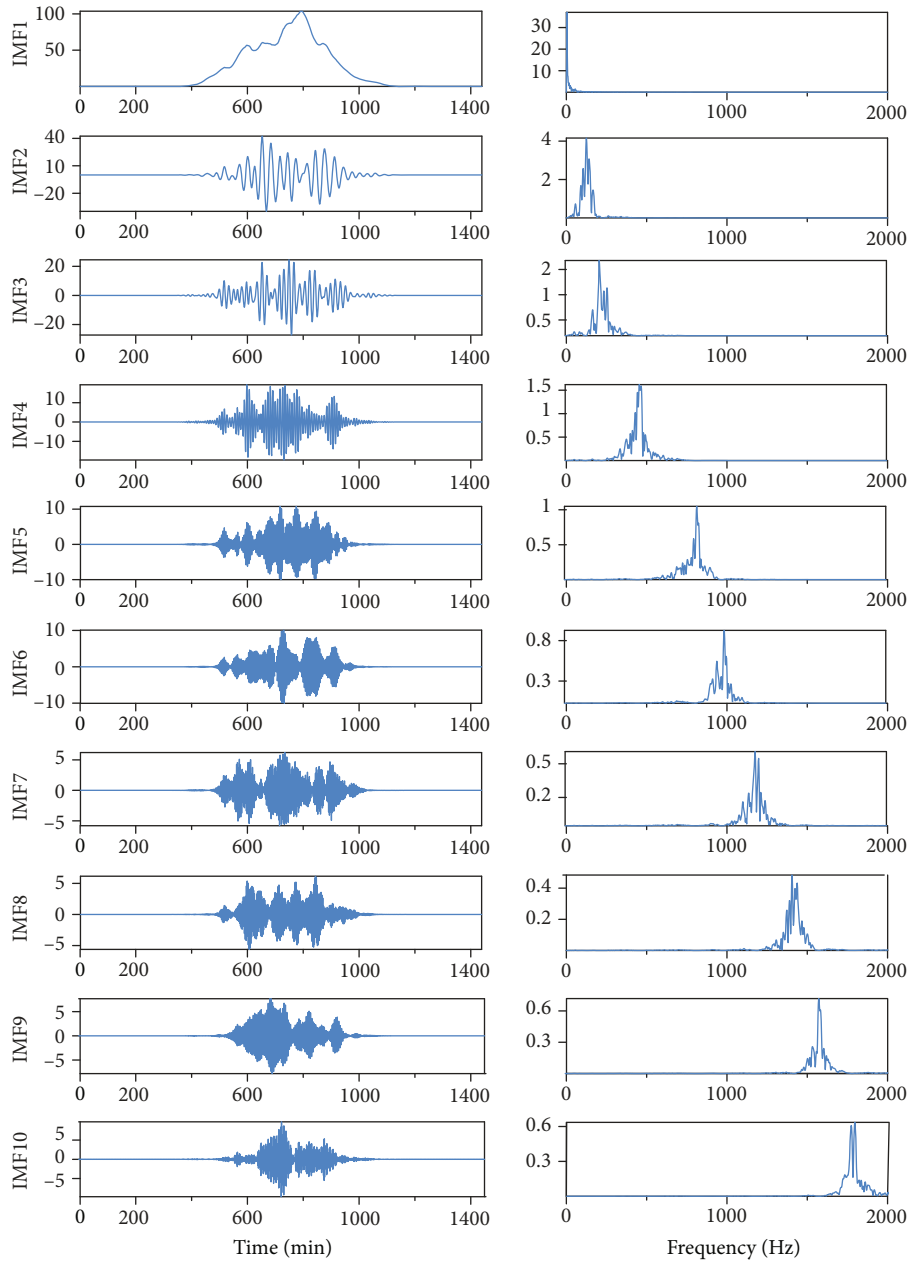

Figure 8: IHHO-VMD decomposition results.

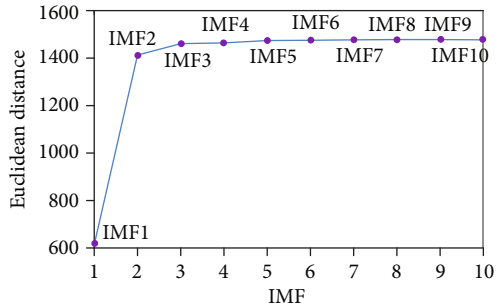

Figure 9: Euclidean distance between each mode and photovoltaic output power.

j is the decomposition point of the correlated and uncorrelated modes. The Euclidean distance formula between two-dimensional vectors, $(x_{11}, x_{12,}\cdots,x_{1n})$ and $(x_{21}, x_{22,}\cdots,x_{2n})$, is

$$d = \sqrt{\sum_{j=1}^{n} \left(x_{1j} - x_{2j}\right)^2}. \tag{20}$$

As can be seen from Figure 8, as the number of submodal decomposition increases, the frequency of submodal components also increases, but the IHHO-VMD decomposition effectively alleviates the submodal aliasing

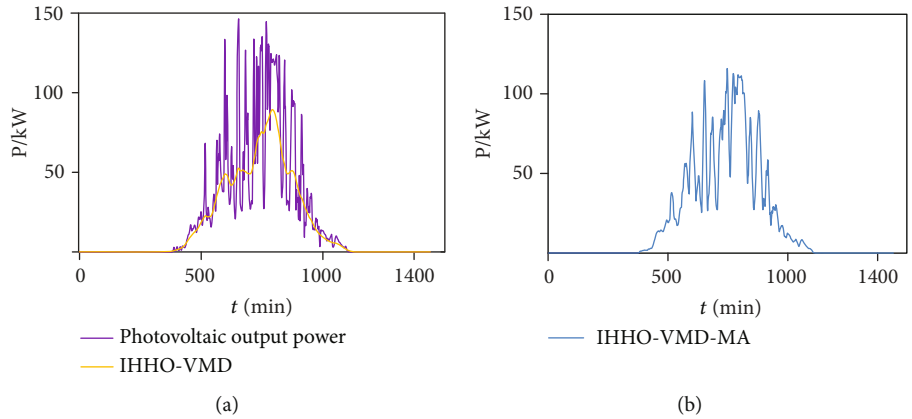

Figure 10: Comparison of PV output power. (a) Grid-connected power with correlated mode. (b) Method of grid-connected power.

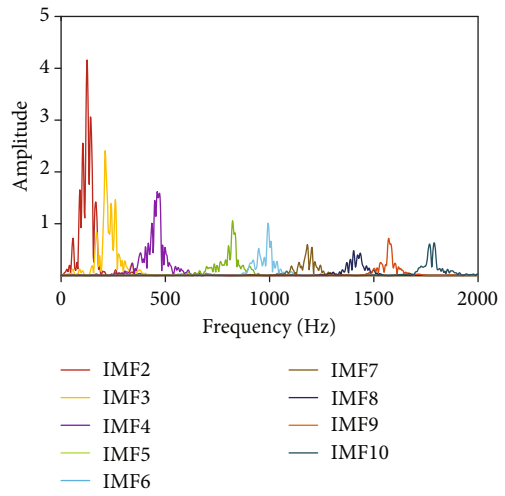

Figure 11: IHHO-VMD-MA spectrum diagram.

phenomenon and has better separation and robustness. According to Formula (20), the Euclidean distance between each submodal component and the original signal is obtained. It can be seen from Figure 9 that the slope between IMF1 and IMF2 is the largest, so IMF1 is used as the correlation mode, while the others are used as the noncorrelation mode.

4.3.2. Selection Analysis of Uncorrelated Modes. In this paper, for the processing of uncorrelated modes, reference [28] moving average method is used to extract the continuous component signals in uncorrelated modes. On the basis of the simple average method, the moving average is calculated by increasing and decreasing the old and new data in sequence. The calculation formula of the moving average method is as follows:

$$\begin{cases} P_{st} = \dfrac{\left(P_{umt-(N/2-1)} + P_{umt-(N/2-2)} + \cdots P_{umt+N/2}\right)}{N}, \\ P_{qt} = P_{umt} - P_{st}, \\ t = N/2, (N/2)+1, \cdots, M-(N/2), \end{cases} \tag{21}$$

where P_{st} represents the continuous component signal of the uncorrelated mode at time t, P_{umt} represents the uncorrelated modal signal at time t, P_{qt} represents the wave component signal of the uncorrelated mode at time t, N represents the length of moving average period, and M represents the number of points measured.

5. Capacity Optimization Model of Hybrid Energy Storage System

5.1. Objective Function. A function is established to minimize the annual comprehensive cost of the hybrid energy storage system, and Formulas (22) and (23) are calculated in the following:

$$\min C = C_B + C_C + C_{Bom} + C_{Com}, \tag{22}$$

$$\begin{cases} C_B = (k_{BP}P_B + k_{BE}E_B)\dfrac{\gamma(1+\gamma)^{T_B}}{(1+\gamma)^{T_B}-1}, \\ C_C = (k_{CP}P_C + k_{CE}E_C)\dfrac{\gamma(1+\gamma)^{T_C}}{(1+\gamma)^{T_C}-1}, \\ C_{Bom} = k_{Bom}E_B, \\ C_{Com} = k_{Com}E_C, \end{cases} \tag{23}$$

where C is the annual comprehensive cost of the hybrid energy storage system; C_B, C_C, C_{Bom}, and C_{Com} are equal annual investment costs and annual operation and maintenance costs of battery and supercapacitor; P_B, P_C, E_B, and E_C are rated power and rated capacity of the battery and supercapacitor; K_{BP}, K_{CP}, K_{BE}, and K_{CE} are power cost coefficient and capacity cost coefficient of battery and supercapacitor; K_{Bom} and K_{Com} are the operation and maintenance cost coefficients of battery and supercapacitor; γ is the discount rate; and T_B and T_C are the service life of the battery and supercapacitor.

5.2. Constraint Conditions

5.2.1. Energy Conservation Constraints. Power should meet the energy conservation; the difference between photovoltaic

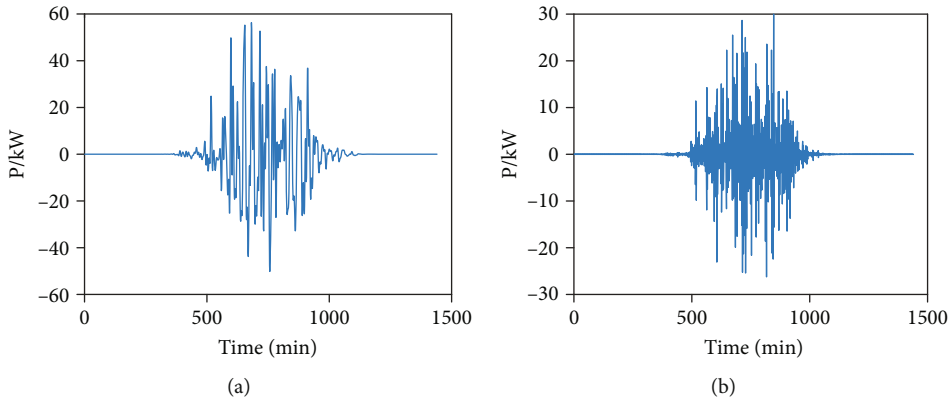

Figure 12: Hybrid energy storage power curve. (a) Battery power. (b) Supercapacitor power.

output power and grid input power should be consistent with the hybrid energy storage system output:

$$\begin{cases} P_{\mathrm{HESS}} = P = P_{\mathrm{W}} + P_{\mathrm{O}}, \\ P_{\mathrm{HESS}} = P_{\mathrm{B}} + P_{\mathrm{C}}, \end{cases} \tag{24}$$

where P_{HESS} is the charge and discharge power of hybrid energy storage, P_{W} is the output power of a photovoltaic power generation system, and P_{O} represents grid-connected power.

5.2.2. Energy Storage Charging and Discharging Power Constraint. The real-time output power of the battery and supercapacitor should be within the rated power range:

$$\begin{cases} -P_{\mathrm{B}} \leqslant P_{\mathrm{B}}(t) \leqslant P_{\mathrm{B}}, \\ -P_{\mathrm{C}} \leqslant P_{\mathrm{C}}(t) \leqslant P_{\mathrm{C}}, \end{cases} \tag{25}$$

where P_{B} and P_{C} are the rated power of the battery and supercapacitor; $P_{\mathrm{B}}(t)$ and $P_{\mathrm{C}}(t)$ are the charging and discharging power of the battery and supercapacitor at time t; $P_{\mathrm{B}}(t) \geq 0$ and $P_{\mathrm{C}}(t) \geq 0$ mean the charging of the battery and supercapacitor, respectively; and $P_{\mathrm{B}}(t) \leq 0$ and $P_{\mathrm{C}}(t) \leq 0$ mean battery and supercapacitor discharge, respectively.

5.2.3. SOC Constraints of Energy Storage. The SOC of the battery and supercapacitor should be within the prescribed range:

$$\begin{cases} \mathrm{SOC}_{\mathrm{B-min}} \leqslant \mathrm{SOC}_{\mathrm{B}}(t) \leqslant \mathrm{SOC}_{\mathrm{B-max}}, \\ \mathrm{SOC}_{\mathrm{C-min}} \leqslant \mathrm{SOC}_{\mathrm{C}}(t) \leqslant \mathrm{SOC}_{\mathrm{C-max}}, \end{cases} \tag{26}$$

$$\mathrm{SOC}(t) = \mathrm{SOC}(t-1) - \frac{\eta P(t) \Delta t}{E}, \tag{27}$$

where $\mathrm{SOC}_{\mathrm{B}}(t)$ and $\mathrm{SOC}_{\mathrm{C}}(t)$ are the states of charge of the battery and the supercapacitor at time t, $\mathrm{SOC}_{\mathrm{B-min}}$ and $\mathrm{SOC}_{\mathrm{B-max}}$ are the upper and lower limits of battery state of charge, $\mathrm{SOC}_{\mathrm{C-min}}$ and $\mathrm{SOC}_{\mathrm{C-max}}$ are the upper and lower limits of the supercapacitor state of charge, η is the charge and discharge efficiency of battery and supercapacitor, $P(t)$ is the power at time t, Δt is the sampling interval time, and E is the energy storage capacity.

6. Example Analysis

In this paper, the Euclidean distance method is used to select the uncorrelated mode, and the uncorrelated mode is processed by Formula (21). By reconstructing the uncorrelated mode continuous component signal and the correlated mode signal, the photovoltaic grid-connected power is obtained.

Figure 10(a) shows the method used in reference [29] to directly use the relevant modes as photovoltaic grid-connected power. Therefore, the maximum fluctuation rate of 1 min obtained by IHHO-VMD is 0.92%, which meets the national photovoltaic grid-connected standard. Although the grid-connected curve is relatively smooth, it is quite different from the original photovoltaic output, and the phenomenon of light abandonment is more serious. The method in this paper can be seen in Figure 10(b). The maximum power fluctuation rate of 1 min is 18.2%, which meets the requirements of grid-connected power stipulated by the state, and the grid-connected curve is more consistent with the original photovoltaic output, and the photovoltaic output is more fully utilized. The spectrum of the uncorrelated modal fluctuation component signal is shown in Figure 10.

By observing the spectrum diagram in Figure 11, it can be seen that the low-frequency fluctuation is mainly concentrated in IMF2 ~ IMF4, the high frequency is mainly concentrated in IMF5 ~ IMF10, and the modal aliasing part in IMF4~IMF5 is the least. Therefore, IMF4 is used as the demarcation point. The low frequency is compensated by the battery, and the high frequency is compensated by the supercapacitor.

It can be seen in Figure 12 that BAT compensates for low-frequency power and SC compensates for high-frequency power, and the distribution results also conform to the response characteristics of BAT and SC. At the same time, the switching times of BAT between charge and discharge are significantly less than that of SC, which plays a significant role in prolonging the battery life.

Table 3: Related parameters of the energy storage system.

Performance index	BAT	SC
Power cost coefficient (CNY/kW)	1500	1500
Capacity cost coefficient (CNY/(kWh))	1000	27000
Operational cost coefficient (CNY/(kWh))	0.05	0.05
Charge discharge efficiency (%)	80	90
SOC upper and lower limits	(0.2, 0.8)	(0.05, 0.95)
Discount rate (%)	10	0

Table 4: The results obtained by configuring different methods.

Method	Energy storage type	Nominal power (kW)	Rated capacity (kWh)	Allocation cost (CNY)
AOA-VMD-MA	BAT	62.71	151.45	88374
	SC	29.27	12.18	
HHO-VMD-MA	BAT	55.99	130.46	76126
	SC	27.94	11.18	
IHHO-VMD-MA	BAT	51.21	123.16	71447
	SC	27.25	10.38	

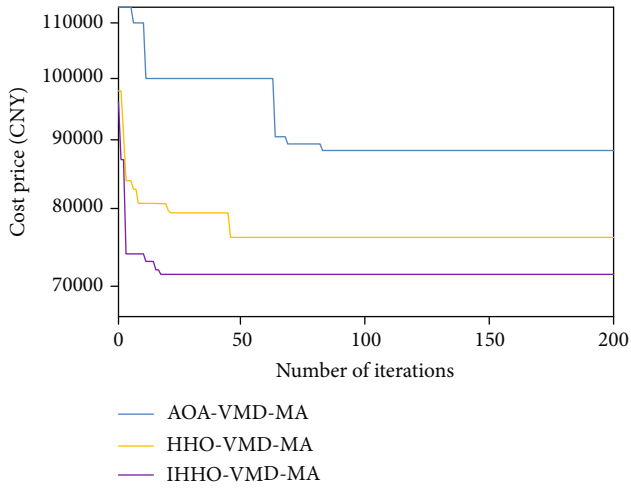

Figure 13: Convergence curves of different methods.

The parameters calculated by the hybrid energy storage system [30, 31] are shown in Table 3. According to the annual average configuration cost and constraints of the energy storage system, IHHO is used to solve the annual average cost of a hybrid energy storage capacity configuration system. In order to verify the effectiveness of the proposed method, this paper compares it with the Harris hawk algorithm to optimize VMD (HHO-VMD-MA) and the arithmetic optimization algorithm to optimize VMD (AOA-VMD-MA). The different method configuration results are shown in Table 4.

As shown in Figure 13 and Table 4, the IHHO-VMD-MA method adopted in this paper can reduce the capacity configuration of HESS and the configuration cost of the energy storage power station. Compared with the HHO-VMD-MA method, the power configuration of BAT decreased by 8.54%, the power configuration of SC decreased by 2.47%, and the annual configuration decreased by 6.15%. Compared with AOA-VMD-MA, the power configuration of BAT decreased by 18.34%, the power configuration of SC decreased by 6.90%, and the annual configuration decreased by 19.15%. The results show that the method adopted in this paper can effectively reduce the economic cost.

7. Conclusions

Aiming at the fluctuation of photovoltaic output power, this paper proposes IHHO to optimize VMD parameters to allocate hybrid energy storage power and draws the following conclusions:

(1) By dividing the photovoltaic output power into correlated mode and uncorrelated mode and using MA to connect the continuous component and correlated mode in the uncorrelated mode to the grid, the power-type energy storage material SC bears the high-frequency part of the power, and the energy-type energy storage material BAT bears the low-frequency part of the power, which can reduce the number of battery charging and discharging times and effectively prolong the service life of the battery

(2) The combination of VMD and MA smooths the power of unrelated modes in P_P and decomposes on the basis of meeting the upper limit of grid-connected volatility stipulated by national standards. Compared with the traditional variational mode decomposition, it is more effective to improve the stability of photovoltaic grid-connected power

(3) Compared with the traditional HHO, the improved IHHO can effectively jump out of the local optimal solution and improve the accuracy and convergence speed of the algorithm. The annual configuration cost is reduced from 76126 CNY to 71447 CNY, a decrease of 6.15%

The proposed MA can effectively suppress the fluctuation of photovoltaic grid-connected power. However, there may be a phenomenon of limiting photovoltaic output power and reducing the power generation of photovoltaic power stations.

It is recommended that further research be undertaken in the following aspects:

(1) In the part of photovoltaic power decomposition, better methods can be explored and adopted to reduce the phenomenon of light abandonment. For example, the application of the Kalman filter in suppressing photovoltaic fluctuations

(2) In this paper, BAT and SC are used as HESS, and there are some limitations in energy storage capacity. In the future, electric hydrogen can be used as part of HESS to reduce environmental pollution and reduce economic costs

Abbreviations

VMD: Variational mode decomposition
HHO: Harris hawks optimization algorithm
AOA: Arithmetic optimization algorithm
EMD: Empirical mode decomposition
EEMD: Ensemble empirical mode decomposition
K: Number of decomposition modes
α: Bandwidth limitation
MA: The moving average method
HESS: Hybrid energy storage system
BAT: Battery
SC: Supercapacitor
PV: Photovoltaics
P_{PV}: Photovoltaic output power
P_{ref}: Input power of the grid
P_{HESS}: HESS charge and discharge power
P_{BAT}: BAT charge and discharge power
P_{SC}: SC charge and discharge power
P_W: Output power of photovoltaic power generation system
P_O: Grid power
C_{0-3}: DC/DC converter
V_t: PV power fluctuation rate within t
$P_{t\ min}, _{t\ max}$: The minimum and maximum output power in t
$P_{capacity}$: Rated installed capacity
F: Original signal
u_k: Modal components after decomposition
$u_k(t)$: Modal component at time t
IMF: Intrinsic mode functions
ω_k: The center frequency of each modal component
$\delta(t)$: Unit impulse function
*: Convolution symbol
λ: Lagrangian multiplier
τ: Noise tolerance of λ
ε: Convergence error
$X(t+1)$: Eagle update location
$\Delta X(t)$: The difference between the current position of prey and the eagle
O: Prey escape energy
D: The number required
S: Random vector
Y: Eagle's next action evaluation indicators
J: Jump intensity
R: A random number between 0 and 1
$X_m(t)$: The average value of the eagle group
X_{best}: Global best position
ω: Adaptive weight factor
T: Maximum number of iterations
t: Current number of iterations
EE: Envelope entropy
$IMF_{i,j}$: The jth sampling point of the ith modal component
N: The length of modal component signal
$p_{i,j}$: Normalized modal component envelope
$IMF_{EE}(i)$: MEE of the ith modal component
d: Euclidean distance theorem
P_{st}: Persistent component signal of uncorrelated mode at time t
P_{umt}: Uncorrelated modal signal at time t
P_{qt}: Wave component signal of uncorrelated mode at time t
N: Moving average period length
M: Number of points measured
C_B, C_C, C_{Bom}, and C_{Com}: Annual comprehensive cost of HESS of BAT and SC
P_B, P_C, E_B, and E_C: Rated power and capacity of BAT and SC
K_{BP}, K_{CP}, K_{BE}, and K_{CE}: Power cost coefficient and capacity cost coefficient of BAT and SC
K_{Bom}, K_{Com}: Operation and maintenance cost coefficient of BAT and SC
γ: Discount rate
T_B, T_C: Useful life of BAT and SC
$SOC_B(t)$ and $SOC_C(t)$: The state of charge of BAT and SC at time t
SOC_{B-min} and SOC_{B-max}: The upper and lower limits of BAT state of charge
SOC_{C-min} and SOC_{C-max}: The upper and lower limits of SC electrical state
η: Charge and discharge efficiency of batteries and supercapacitors
Δt: Sampling interval time
E: Energy storage capacity
$X_{rabbit}(t)$: Position vector of prey
$X(t)$: The current location of the eagle.

Data Availability

The data used to support the findings of this study are available from the corresponding author upon request.

Conflicts of Interest

The authors declare that there is no conflict of interest regarding the publication of this paper.

Acknowledgments

This work was supported by the Open Research Fund of Guangxi Key Laboratory of Building New Energy and Energy Conservation (Gui Keneng 17-J-21-4).

References

[1] Y. Li, T. Y. Yao, X. B. Qiao, J. X. Xiao, and Y. J. Cao, "Optimal configuration of distributed photovoltaic and energy storage system based on joint sequential scenario and source-network-load coordination," *Transactions of Chinese Electrotechnical Society*, vol. 30, no. 28, pp. 12–18, 2021.

[2] S. Garip and S. Ozdemir, "Optimization of PV and battery energy storage size in grid-connected microgrid," *Applied Sciences*, vol. 12, no. 16, p. 8247, 2022.

[3] X. S. Tang, Y. S. Sun, G. P. Zhou, and F. F. Miao, "Coordinated control of multi-type energy etorage for wind power fluctuation suppression," *Energies*, vol. 10, no. 8, p. 1212, 2017.

[4] M. T. Zhang, S. Tian, and Z. H. Zeng, "Optimal allocation of hybrid energy storage capacity based on variational mode decomposition," *Energy Storage Science and Technology*, vol. 9, no. 1, pp. 170–177, 2020.

[5] J. H. Li, Y. N. Fu, C. P. Li, J. Li, Z. Xing, and T. Ma, "Improving wind power integration by regenerative electric boiler and battery energy storage device," *International Journal of Electrical Power & Energy Systems*, vol. 131, article 107039, 2021.

[6] R. Du, P. H. Zou, and C. Ma, "Multi-objective optimal sizing of hybrid energy storage systems for grid-connected wind farms using fuzzy control," *Journal Renewable and Sustainable Energy*, vol. 13, no. 1, article 014103, 2021.

[7] J. Tang and Y. H. Jiang, "Hybrid energy storage capacity allocation based on adaptive wavelet transform and HHT," *Journal of Power Supply*, vol. l45, no. 2, pp. 32–38, 2017.

[8] L. Cheng and F. H. Zhang, "Wavelet transform method for hybrid energy storage system smoothing power fluctuation," *Electric Power Automation Equipment*, vol. 41, no. 3, pp. 100–104, 2021.

[9] J. H. Zhang and Y. D. Hu, "Optimization strategy for hybrid energy storage power distribution based on fuzzy control," *Journal of Physics: Conference Series*, vol. 1549, no. 5, article 052115, 2020.

[10] G. Xiao, F. Xu, L. H. Tong, H. R. Xu, and P. W. Zhu, "A hybrid energy storage system based on self-adaptive variational mode decomposition to smooth photovoltaic power fluctuation," *Journal of Energy Storage*, vol. 55, article 105509, 2022.

[11] Q. Zhang, J. J. Wu, Y. Ma, G. Li, J. Ma, and C. Wang, "Short-term load forecasting method with variational mode decomposition and stacking model fusion," *Sustainable Energy, Grids and Networks*, vol. 30, article 100622, 2022.

[12] S. Rahman, S. Saha, M. E. Haque et al., "A framework to assess voltage stability of power grids with high penetration of solar PV systems," *International Journal of Electrical Power & Energy Systems*, vol. 139, article 107815, 2022.

[13] P. Singh and J. S. Lather, "Dynamic power management and control for low voltage DC microgrid with hybrid energy storage system using hybrid bat search algorithm and artificial neural network," *Journal of Energy Storage*, vol. 32, article 0191574, 2020.

[14] Z. M. Liu, G. Y. Qi, J. G. Gao, and Z. G. Wang, "Research on optimal configuration of hybrid energy storage capacity based on adaptive VMD," *Acta Energies Solaris Sinica*, vol. 43, no. 4, pp. 75–81, 2022.

[15] X. Zhang, Q. Miao, H. Zhang, and L. Wang, "A parameter-adaptive VMD method based on grasshopper optimization algorithm to analyze vibration signals from rotating machinery," *Mechanical Systems and Signal Processing*, vol. 108, pp. 58–72, 2018.

[16] P. Q. Li, X. Li, S. Cai, W. Zhao, and E. T. Lei, "Capacity Optimization Configuration of Hybrid Energy Storage System With Retired Power Batteries in Wind Farms," *Acta Energies Solaris Sinica*, vol. 43, no. 5, pp. 492–498, 2022.

[17] W. Ma, W. Wang, X. Z. Wu, R. Hu, F. Tang, and W. Zhang, "Control strategy of a hybrid energy storage system to smooth photovoltaic power fluctuations considering photovoltaic output power curtailment," *Sustainability*, vol. 11, no. 5, p. 1324, 2019.

[18] W. W. Tian, L. X. Lu, X. K. Feng, and Z. Q. Wang, "Condition monitoring of wind turbine gearbox based on improved AAKR," *Electronic Measurement Techniques*, vol. 45, no. 15, pp. 158–165, 2022.

[19] W. D. Zhang, Z. M. Liu, and L. X. Shen, "Research on photovoltaic flexible grid connection using energy storage to smooth fluctuation," *Electric Power Automation Equipment*, vol. 33, no. 5, pp. 106–111, 2013.

[20] K. Dragomiretskiy and D. Zosso, "Variational mode decomposition," *IEEE Transactions on Signal Processing*, vol. 62, no. 3, pp. 531–544, 2014.

[21] X. An and J. Yang, "Denoising of hydropower unit vibration signal based on variational mode decomposition and approximate entropy," *Transactions of the Institute of Measurement and Control*, vol. 38, no. 3, pp. 282–292, 2016.

[22] A. A. Heidari, S. Mirjalili, H. Faris, I. Aljarah, M. Mafarja, and H. Chen, "Harris hawks optimization: algorithm and applications," *Future Generation Computer Systems*, vol. 97, pp. 849–872, 2019.

[23] L. L. Bai, X. N. Yang, J. Y. Zhang, W. F. Sun, and H. L. Chen, "Optimal configuration of distributed power supply based on improved Harris eagle algorithm," *Journal of Jilin University*, vol. 40, no. 5, pp. 734–743, 2022.

[24] J. Y. Li and T. Y. Ma, "Short-term grid load forecasting based on CEHHO-KELM," *Electric Power Science and Engineering*, vol. 39, no. 1, pp. 52–60, 2023.

[25] W. X. Gao, S. Liu, Z. Y. Xiao, and J. F. Yu, "Butterfly optimization algorithm based on Cauchy variation and adaptive weight," *Computer Engineering and Applications*, vol. 56, no. 15, pp. 43–50, 2020.

[26] Y. Yuan, C. C. Sun, M. T. Li, S. S. Choi, and Q. Li, "Determination of optimal supercapacitor-lead-acid battery energy storage capacity for smoothing wind power using empirical mode decomposition and neural network," *Electric Power Systems Research*, vol. 127, pp. 323–331, 2015.

[27] J. Y. Lu, X. Qu, D. M. Wang, J. K. Yue, L. J. Zhu, and G. F. Li, "Signal filtering method of variational mode decomposition and Euclidean distance based on optimizing parameters of classification particle swarm optimization algorithm," *Transactions of the Institute of Measurement and Control*, vol. 43, no. 9, pp. 2018–2029, 2021.

[28] Y. Wang, L. Lv, and Y. W. Zu, "Capacity configuration of hybrid energy storage system based on double layer power decomposition," *Electric Power Construction*, vol. 37, no. 12, pp. 61–67, 2016.

[29] Y. H. Xu and Y. J. Xu, "Capacity configuration and control strategy of hybrid energy storage to smooth wind power fluctuations," *High Voltage Apparatus*, vol. 54, no. 6, pp. 186–193, 2022.

[30] C. H. Kebin, Q. I. Xiaoyan, and Z. H. Jinshuai, "Sizing and cost analysis of hybrid energy storage system for compensating wind power forecast errors," *High Voltage Apparatus*, vol. 54, no. 6, pp. 189–196, 2018.

[31] M. Pang, Y. Shi, W. Wang, and S. Pang, "Optimal sizing of hybrid energy storage system taking into account economic factors and power allocation," *Journal of Northwestern Polytechnical University*, vol. 36, no. 4, pp. 679–684, 2018.